General Disclaimer

One or more of the Following Statements may affect this Document

- This document has been reproduced from the best copy furnished by the organizational source. It is being released in the interest of making available as much information as possible.

- This document may contain data, which exceeds the sheet parameters. It was furnished in this condition by the organizational source and is the best copy available.

- This document may contain tone-on-tone or color graphs, charts and/or pictures, which have been reproduced in black and white.

- This document is paginated as submitted by the original source.

- Portions of this document are not fully legible due to the historical nature of some of the material. However, it is the best reproduction available from the original submission.

NASA TECHNICAL MEMORANDUM

NASA TM X-72778

NASA TM X-72778

SPECTRAL RESPONSE OF THE VIKING LANDER CAMERA: PRELIMINARY EVALUATION

By W. Lane Kelly IV, Friedrich O. Huck,
and Raymond E. Arvidson

NATIONAL AERONAUTICS AND SPACE ADMINISTRATION
LANGLEY RESEARCH CENTER, HAMPTON, VIRGINIA 23665

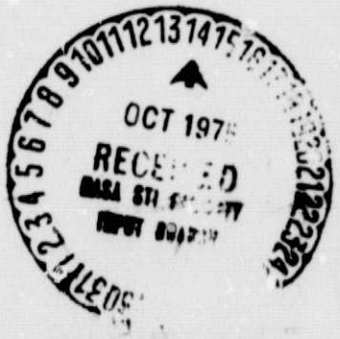

SPECTRAL RESPONSE OF THE VIKING LANDER CAMERA: PRELIMINARY EVALUATION

By

W. Lane Kelly IV, Friedrich O. Huck,

and Raymond E. Arvidson*

SUMMARY

One of the objectives of the Viking lander imaging investigation is to obtain color and near-infrared multispectral panoramas of the Martian surface using six spectral channels in the 0.4 to 1.1 μm wavelength range. This data can be compared with data obtained by imaging a reference test chart to construct approximate spectral reflectance curves that can then be matched to laboratory standards to aid in identifying surface materials. Unfortunately, some of these channels exhibit appreciable out-of-band spectral responses, making data reduction and interpretation a more difficult task than might be initially assumed.

A preliminary evaluation of predicted multispectral data for 8 geological materials reveals that fairly good reflectance estimates can be made for those materials which have monotonically increasing or decreasing reflectances. Reflectance estimates for materials with more complex reflectances often do not reveal important spectral features and sometimes provide misleading results. More advanced data reduction techniques must be explored before judging the value of the Viking camera multispectral data for constructing spectral reflectance curves and identifying surface materials.

---

*Washington University, St. Louis, Missouri

INTRODUCTION

The Viking lander cameras (ref. 1) will return stereo views and color and near-infrared multispectral panoramas of the Martian surface with four orders of magnitude higher resolution than has been obtained before. Data from six spectral channels will be compared with data obtained while viewing a reference test chart to construct approximate spectral reflectance curves that can then be matched to laboratory standards to aid in identifying surface materials. Three spectral bands in the visual (0.4 to 0.7 μm) region were selected to produce conventional color images, and three bands in the near-infrared (0.7 to 1.1 μm) to detect reflectance minima near 0.95 μm due to Fe^{2+} and Fe^{3+} electronic transition absorption bands.

Unfortunately, the actual responsivity shapes of the spectral channels depart significantly from the desired goals. Photosensor array size and sterilization requirements dictate the choice of the spectral filters. Glass absorption filters are ineffective in the thickness (0.25 mm) that could be allotted for them, and organic dye absorption filters could not survive sterilization and assembly heat cycles. Only interference type filters could therefore be u[illegible]

Interference [illegible]ters have multiple order transmittance peaks, and are most readily made with very narrow-band transmittances (about 0.1 μm for visible wavelength filters). However, the camera filters were desired to have transmittance half widths of 0.05 to 0.1 μm, with an average pass band transmittance over 65% and with blocking over the range from 0.4 to 1.1 μm. Blocking of the multiple order transmittance peaks was only partially successful, however, and some of the filters exhibit severe out-of-band leakage.

The undesired signal components due to out-of-band responsivity vary appreciably between channels, and may still further increase for some of the near-infrared channels by the time the landers have reached Mars. The cameras are exposed to a steady low flux of neutrons and gamma rays from the lander radioisotope-thermoelectric generators during the nearly one year cruise from Earth to Mars. Radiation damage by the neutrons degrades the photodiode performance, particularly in the infrared region from 0.8 to 1.1 μm where the absolute responsivity could be reduced by an estimated 15 to 40%.

The purpose of this paper is to provide a preliminary evaluation of the camera spectral response. An analytical model of the camera is used to predict camera data for spectral reflectances corresponding to several geological materials. An initial estimate of these spectral reflectances, referred to here as a first-order estimate, is determined by ratioing multispectral imagery data obtained from the surface material and a reference test chart. This ratio avoids uncertainties which are associated with absolute radiometric measurements (ref. 2). A second estimate of surface reflectance, referred to here as a second-order estimate, is determined by using the first-order reflectance curve to evaluate the out-of-band signal components and subtracting these components from the total signal. Both first and second-order results are compared to the input spectral reflectances.

SYMBOLS

D	lens diameter, m
DN	digital number
G	gain of PSA channel
g	phase angle, deg

k_c	PSA channel calibration factor
k_{co}	commandable offset constant
k_g	gain constant
k_o	offset constant
$R(\lambda)$	PSA channel responsivity
R_f	preamplifier feedback resistance
$S(\lambda)$	solar irradiance
V	PSA output voltage
β	instantaneous field of view, deg, or radians
ϵ	angle between emitted radiation and normal to surface, deg
i	angle between incident radiation and normal to surface, deg
Ω	desired spectral bandwidth, μm
λ	wavelength, μm
$\rho(\lambda)$	spectral reflectivity of surface (normal albedo)
$\tau_a(\lambda)$	spectral transmittance of atmosphere
$\tau_o(\lambda)$	spectral transmittance of camera optics
ϕ	illumination scattering function
<>	estimate

Subscripts:

i	PSA channel
j	target surface
m	Martian surface
r	reference test chart patch

MULTISPECTRAL DATA

Camera Responsivity

Figure 1 shows a cut-away view of the Viking lander camera. Light from the scene is reflected by a scanning mirror to an objective lens which images this light onto a plane that contains an array of photosensors, each covered by a small aperture. The photosensors convert the light into an electrical signal which is amplified, sampled, and quantized for digital transmission. The camera rotates a small step in azimuth between elevation line scans until the entire scene of interest is scanned.

The camera features an array of 12 silicon photodiodes, consisting of four broadband channels with selectable focus for high-resolution imaging, one broadband channel for low-resolution surveys, six narrowband channels for multispectral imaging (color and near-infrared), and one narrowband channel for scanning the sun. Typical responsivities are plotted in figure 2. The instantaneous fields of view are 0.04° for the high-resolution channels and 0.12° for the other channels.

Figure 3 shows a simplified circuit diagram of the photosensor array (PSA) and video processing electronics (VPE). The PSA output voltage may be formulated as (ref. 2)

$$V_{ij} = \frac{\pi}{16} \beta_i^2 D^2 k_{ci} R_{fi} G_i \int_0^{\infty} S(\lambda)\tau_a(\lambda)\rho_j(\lambda)\phi_j(\iota,\varepsilon,g)\tau_c(\lambda)R_i(\lambda)d\lambda \qquad (1)$$

where the subscript i refers to the selected PSA channel, and the subscript j to the target being imaged. The parameter β is the instantaneous field of view, D the lens aperture diameter, k_c a radiometric calibration factor for each PSA channel, R_f the preamplifier feedback resistance, G the channel

gains, $\tau_c(\lambda)$ the camera optical throughput, and $R(\lambda)$ the PSA responsivity. Values for flight camera 1B, which is used here as example, are listed in Tables I and II.

The target radiance depends on the solar irradiance $S(\lambda)$, the atmospheric transmittance $\tau_a(\lambda)$, and the surface albedo $\rho_j(\lambda)$ and illumination scattering function $\phi_j(\iota,\epsilon,g)$. The subscript j becomes m for the Martian surface and r for the reference test chart. The illumination scattering function is assumed to be independent of wavelength. This assumption is approximately valid for the 11 grey patches of the reference test chart, which is shown in figure 4, but may not be completely valid for the Martian surface.

To further characterize the camera responsivity and illustrate the magnitude of the out-of-band signals, figure 5 presents a plot of the product of solar irradiance, atmospheric transmissivity, camera optical throughput, and PSA responsivities (i.e., $S(\lambda)\tau_a(\lambda)\tau_c(\lambda)R(\lambda)$) versus wavelength. These curves clearly indicate that the Green, Red, and IR1 channels should provide the more accurate spectral information, whereas the other three channels, especially IR3, are appreciably contaminated with out-of-band signals.

The PSA output voltage V_{ij} is passed either directly (for the rapid-scan mode) or through a 200-Hz low-pass filter (for the slow-scan mode) to circuits which provide commandable gains and offsets, automatic dark current subtraction, and analog-to-digital (A/D) conversion. The voltage V_{ij} may be estimated from the transmitted digital number, DN_{ij}, by the expression (ref. 2)

$$\langle V_{ij} \rangle = DN_{ij} \frac{2^{G.n.}}{k_g} + k_{co}O.n. - k_o \qquad (2)$$

where G.n. and O.n. are commandable gain and offset numbers, respectively, as illustrated in figure 6; k_g(=444.321) is a gain constant, and k_{co} (=0.1441) and k_o(=0.204) are offset constants. Electronic and quantization noise introduce some error into this signal voltage estimate. The electronic noise can be reduced by averaging data obtained from repeated line scans, and the quantization noise can be reduced by selecting a low gain number once the scene radiance has been approximately determined from initial pictures.

Input and Output Data

The absolute spectral reflectances or albedoes, $\rho_m(\lambda)$, of 8 possible targets shown in figure 7 are used as input data in predicting camera output data. The reflectance test chart patches are assumed to be spectrally flat. Solar irradiance $S(\lambda)$, and atmospheric transmittance $\tau_a(\lambda)$ are listed in Table III.

The first step is to compute the PSA signal output voltages V_{ij} using equation (1). The second step is to compute the corresponding digital numbers DN_{ij}, using optimum gains and offsets. The last step is to estimate the PSA output, $\langle V_{ij} \rangle$, using equation (2), as will have to be done also with actual camera data. Results of each step are listed in Table IV for one of the spectral reflectances (average Mars) to illustrate computations.

If the PSA voltages V_{mi} and V_{ri} are digitized with the same gain and offset, as is simulated here, then errors in the gain and offset constants of equation (2) have only a small effect on the estimated ratio $\frac{\langle V_{mi} \rangle}{\langle V_{ri} \rangle}$. There is a sufficiently wide range of grey patch reflectances available so that a reflectance can always be found for which $V_{mi} \approx V_{ri}$ (ref. 2).

FIRST-ORDER ESTIMATE OF SPECTRAL REFLECTIVITY

Basic to any multispectral data reduction technique is the requirement that the camera image a reference test chart in addition to the scene of interest. However, it is not necessary that the scene and chart are viewed at a similar lighting and viewing geometry. Only the PSA output voltages from the six spectral channels relative to each other are used to avoid the uncertainties associated with absolute radiometry.

According to equation (1), the first-order estimate of the absolute surface reflectance in the i'th spectral channel is

$$\langle \rho_{ij} \rangle^{I} \phi_j(\iota,\varepsilon,g) = \frac{\langle V_{ij} \rangle}{\frac{\pi}{16} \beta_i^2 D^2 k_{ci} R_{fi} G_i \int_0^\infty S(\lambda)\tau_a(\lambda)\tau_c(\lambda)R_i(\lambda)d\lambda} \tag{3}$$

It follows that the first-order estimate of the reflectance of a Martian surface element relative to a grey patch of the reference test chart is

$$\frac{\langle \rho_{mi} \rangle^{I} \phi_m(\iota,\varepsilon,g)}{\rho_{ri} \phi_r(\iota,\varepsilon,g)} = \frac{\langle V_{mi} \rangle}{\langle V_{ri} \rangle} = \left\langle \frac{V_{mi}}{V_{ri}} \right\rangle^{I} \tag{4}$$

The ratio $\frac{\phi_m(\iota,\varepsilon,g)}{\phi_r(\iota,\varepsilon,g)}$, being assumed independent of wavelength, is constant for all spectral data that has been obtained with the same lighting and viewing geometry. This is always true for the three color channels with respect to each other, and similarly for the three near-infrared channels, because of the line-sequential imaging technique of the Viking lander cameras (ref. 1). However, this is true for the color and near-infrared channels with respect to each other only if images are obtained under identical lighting and viewing geometry. Otherwise, the illumination scattering

function of the surface would have to be accounted for.

Given these simplifying conditions, the first-order estimate of the reflectance of a Martian surface element in the i'th spectral channel becomes

$$\langle\tilde{\rho}_{mi}\rangle^{I} = \left\langle\frac{V_{mi}}{V_{ri}}\right\rangle^{I} \tilde{\rho}_{ri} \qquad (5)$$

It is important to carefully select the wavelengths at which to plot these estimates. Two approaches are illustrated. A simplistic approach is to select these wavelengths simply near the in-band response of each channel, and listed in Table IV as $\bar{\lambda}_i^{II}$. Results of this approach are illustrated in figure 8, where the values $\langle\tilde{\rho}_{mi}\rangle^{I}$ are connected by a smooth curve. (Of course, a wide range of curves could have been drawn). Several striking discrepancies between the input and reconstructed reflectance curves can be readily observed. Reflectance minima around 0.95 μm appears in one of the reflectance estimates (olivine) although not present in the input data. The three IR channels were specifically selected to detect reflectance minima near 0.95 μm due to iron electronic transition absorption bands. Ironically, the simplistic approach of selecting wavelengths at which to reconstruct the estimates $\langle\tilde{\rho}_{mi}\rangle^{I}$ can lead to the conclusion that such absorption bands are present when in fact they are not.

An unbiased, or objective, estimate of the wavelengths at which the values $\langle\tilde{\rho}_{mi}\rangle^{I}$ should be plotted is the surface-irradiance and camera-responsivity weighted wavelength

$$\bar{\lambda}_i^{I} = \frac{\int_0^{\infty} \lambda\, S(\lambda)\tau_a(\lambda)\tau_c(\lambda)R_i(\lambda)d\lambda}{\int_0^{\infty} S(\lambda)\tau_a(\lambda)\tau_c(\lambda)R_i(\lambda)d\lambda} \qquad (6)$$

The resulting wavelengths are listed in Table IV. It should be noted that $\lambda_{IR3} < \lambda_{IR2}$.

Figure 9 presents the estimates $\langle\tilde{\rho}_{mi}\rangle^I$ plotted as a function of λ_i^I and connected by a smooth curve. Data points plotted in figure 9 show close agreement with the input curves, and materials with monotonically increasing or decreasing curves are now well represented. However, the curves with interesting spectral features between 0.7 and 1.1 μm, such as the 0.95 μm iron absorption band, cannot be accurately represented. This result is an outcome as much from undersampling the reflectance variations as from out-of-band response.

SECOND-ORDER ESTIMATE OF SPECTRAL REFLECTIVITY

The magnitude of the undesired signal component for the reference test chart data may be estimated as

$$\langle V_{ri}\rangle|_{\lambda\notin\Lambda_i} = \frac{\pi}{16}\beta_i^2 D^2 k_{ci} R_{fi} G_i \phi_r(\iota,\varepsilon,g) \int_{\lambda\notin\Lambda_i} S(\lambda)\tau_a(\lambda)\rho_r(\lambda)\tau_c(\lambda)R_i(\lambda)d\lambda \qquad (7)$$

where Λ_i is the desired spectral bandwidth of the i'th channel. The integration occurs over all wavelengths outside this bandwidth. Similarly, the undesired signal component for the Martian surface data may be estimated as

$$\langle V_{mi}\rangle|_{\lambda\notin\Lambda_i} = \frac{\pi}{16}\beta_i^2 D^2 k_{ci} R_{fi} G_i \phi_m(\iota,\varepsilon,g) \int_{\lambda\notin\Lambda} S(\lambda)\tau_a(\lambda)\langle\rho_m(\lambda)^I\rangle\tau_c(\lambda)R_i(\lambda)d\lambda \qquad (8)$$

As before, to avoid the uncertainties associated with absolute radiometry, data from the surface can be ratioed to the reference test chart to obtain the second-order spectral reflectance estimate

$$\langle \tilde{\rho}_{mi} \rangle^{II} = \left\langle \frac{V_{mi}}{V_{ri}} \right\rangle^{II} \tilde{\rho}_{ri} \tag{9}$$

where

$$\left\langle \frac{V_{mi}}{V_{ri}} \right\rangle^{II} = \frac{\int_0^\infty S(\lambda)\tau_a(\lambda)\langle \tilde{\rho}_m(\lambda) \rangle^{I} \tau_c(\lambda) R_i(\lambda) d\lambda - \int_{\lambda \notin \Lambda_i} S(\lambda)\tau_a(\lambda)\langle \tilde{\rho}_m(\lambda) \rangle^{I} \tau_c(\lambda) R_i(\lambda) d\lambda}{\int_0^\infty S(\lambda)\tau_a(\lambda)\tilde{\rho}_r(\lambda)\tau_c(\lambda) R_i(\lambda) d\lambda - \int_{\lambda \notin \Lambda_i} S(\lambda)\tau_a(\lambda)\tilde{\rho}_r(\lambda)\tau_c(\lambda) R_i(\lambda) d\lambda}$$

The corresponding unbiased estimate of the wavelengths at which the values $\langle \tilde{\rho}_{mi} \rangle^{II}$ should be plotted is

$$\lambda_i^{II} = \frac{\int_{\lambda \in \Lambda_i} \lambda\, S(\lambda)\tau_a(\lambda)\, \tau_c(\lambda) R_i(\lambda) d\lambda}{\int_{\lambda \in \Lambda_i} S(\lambda)\tau_a(\lambda)\tau_c(\lambda) R_i(\lambda) d\lambda} \tag{10}$$

where the integral is evaluated over the in-band response.

Figure 10 presents the second-order estimates $\langle \rho_{mi} \rangle^{II}$ plotted at λ_i^{II} and connected by a smooth curve. Second-order results are strongly influenced by the first-order curve fits and second-order results show essentially no improvement over the first-order estimates plotted in figure 9.

CONCLUSIONS

An analytical model of the Viking lander cameras spectral response was used to predict the multispectral data that would be obtained when imaging materials that could reasonably be expected on Mars. First-order estimates of surface spectral reflectance were obtained for each of the 6 spectral channels by ratioing data obtained from imaging these surfaces to data obtained

from imaging a reference test chart under identical lighting and viewing geometry. Second-order estimates were obtained by estimating and then subtracting the contribution of out-of-band signal components.

The following conclusions were reached:

(1) The green, red, and IR1 channel responses generate negligible out-of-band signal; however, the other three channels, especially IR3, are appreciably contaminated.

(2) First-order results provide fairly good reflectance estimates for materials with monotonically increasing or decreasing reflectances at visible wavelengths. Data for the three IR channels continues to provide an approximate fit to simple reflectances only if the data is plotted at solar-irradiance and camera-responsivity weighted wavelengths. Otherwise, serious errors can occur. Perhaps the most notable error that could occur is the appearance of an iron absorption band around 0.95 μm in the estimated reflectance curves that is not present in the material.

(3) For materials with more complex spectral reflectances, such as the iron absorption band, first-order estimates plotted at solar-irradiance and camera-responsivity weighted wavelengths do not reveal these features and often provide misleading results.

(4) Second-order estimates of spectral reflectances provide no appreciable improvements over the first-order estimates. They were strongly influenced by assumptions made to construct spectral curves from the first-order estimates and tended to confirm initial biases.

(5) More advanced data reduction techniques should be explored in order to best utilize the multispectral capability of the Viking lander cameras.

REFERENCES

1. Huck, F. O.; McCall, H. F.; Patterson, W. R.; and Taylor, G. R.: The Viking Mars Lander Camera, Space Science Instrumentation, Vol. 1, No. 2, 1975.

2. Huck, F. O.; Burcher, E. E.; Taylor, E. J.; and Wall, S. D.: Radiometric Performance of the Viking Mars Lander Cameras, NASA TM X-72692, 1975.

TABLE I

RESPONSIVITIES OF FLIGHT CAMERA 1B

WITH PHOTOSENSOR ARRAY M17

λ, μm	Responsivities, A/W						Optical throughput $\tau_c(\lambda)$
	Blue	Green	Red	IR1	IR2	IR3	
.400	.044	.001	.005	.002	.002	.005	.597
.425	.082	.001	.004	.001	.001	.003	.680
.450	.120	.001	.002	.001	.001	.005	.700
.475	.142	.003	.001	.001	.002	.009	.738
.500	.120	.044	.001	.000	.008	.014	.776
.525	.004	.108	.001	.000	.017	.008	.768
.550	.001	.186	.001	.000	.007	.005	.761
.575	.001	.082	.003	.001	.001	.005	.754
.600	.001	.017	.053	.001	.001	.006	.740
.625	.002	.003	.252	.001	.001	.008	.738
.650	.014	.001	.251	.001	.001	.010	.717
.675	.037	.001	.265	.001	.001	.015	.711
.700	.005	.001	.293	.000	.001	.020	.710
.725	.001	.001	.187	.001	.002	.029	.679
.750	.001	.000	.040	.001	.005	.042	.663
.775	.000	.002	.024	.006	.007	.007	.657
.800	.002	.002	.010	.030	.002	.002	.638
.825	.000	.000	.007	.128	.002	.002	.681
.850	.000	.000	.003	.290	.002	.002	.677
.875	.000	.000	.007	.226	.005	.003	.678
.900	.001	.000	.001	.272	.025	.008	.653
.925	.000	.001	.000	.101	.220	.028	.647
.950	.001	.001	.000	.026	.270	.117	.714
.975	.003	.001	.000	.011	.138	.212	.721
1.000	.002	.003	.000	.006	.027	.169	.711
1.025	.002	.002	.001	.004	.010	.121	.723
1.050	.004	.002	.001	.003	.005	.072	.715
1.075	.018	.006	.000	.003	.004	.038	.714
1.100	.034	.016	.000	.004	.004	.020	.716

TABLE II

CHARACTERISTICS OF PHOTOSENSOR ARRAY M17

Channel	k_{ci}	R_{fi} MΩ	G_i
Blue	1.405	735.0	22.7
Green	1.430	709.5	24.5
Red	.446	764.1	7.02
IR1	.821	719.5	14.16
IR2	1.276	707.1	21.93
IR3	1.025	752.2	16.56

TABLE III

AVERAGE MARS RADIANCE DATA AT 1.6 A.U.

λ, μm	$S(\lambda)$, kW/m^2-um	$\tau_a(\lambda)$	$\rho_m(\lambda)$
.400	.602	.890	.058
.425	.738	.906	.066
.450	.859	.921	.074
.475	.859	.938	.083
.500	.773	.954	.092
.525	.750	.960	.106
.550	.762	.965	.119
.575	.731	.971	.133
.600	.707	.977	.146
.625	.672	.979	.163
.650	.633	.981	.180
.675	.598	.983	.197
.700	.562	.985	.214
.725	.529	.987	.219
.750	.496	.989	.225
.775	.469	.991	.225
.800	.441	.992	.225
.825	.416	.992	.224
.850	.391	.992	.223
.875	.370	.993	.223
.900	.349	.993	.223
.925	.332	.993	.219
.950	.314	.993	.216
.975	.298	.993	.215
1.000	.283	.993	.214
1.025	.276	.993	.213
1.050	.260	.993	.212
1.075	.248	.993	.214
1.100	.237	.993	.217

TABLE IV

REPRESENTATIVE VALUES FOR CALCULATION OF FIRST-ORDER SPECTRAL REFLECTANCE

Target		Blue	Green	Red	IR1	IR2	IR3
Average Mars	V_{mi}	1.33	1.44	1.36	1.34	1.57	1.63
	DN_{mi}	19	21	20	19	23	23
	$\langle V_{mi} \rangle$	1.31	1.45	1.38	1.31	1.60	1.60
20% Grey Patch	V_{ri}	2.82	2.41	1.44	1.22	1.54	1.63
	DN_{ri}	40	34	21	18	22	24
	$\langle V_{ri} \rangle$	2.82	2.39	1.45	1.24	1.52	1.67
	$\bar{\lambda}_i^{I}$	.500	.556	.669	.867	.889	.874
	$\bar{\lambda}_i^{II}$	.465	.545	.669	.871	.946	.993

Gain #5, Offset #1

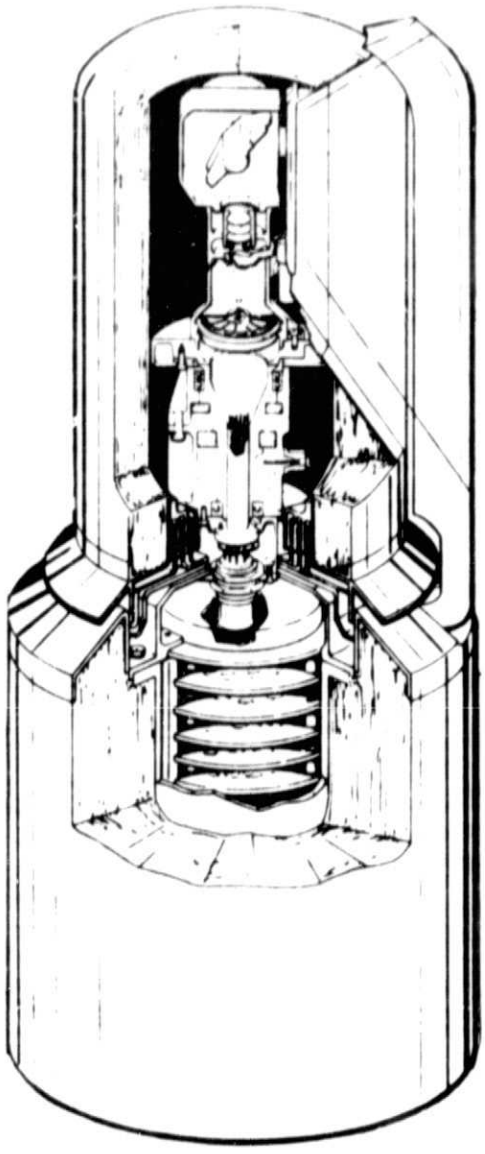

Figure 1.- Simplified cutaway view of the Viking lander camera.

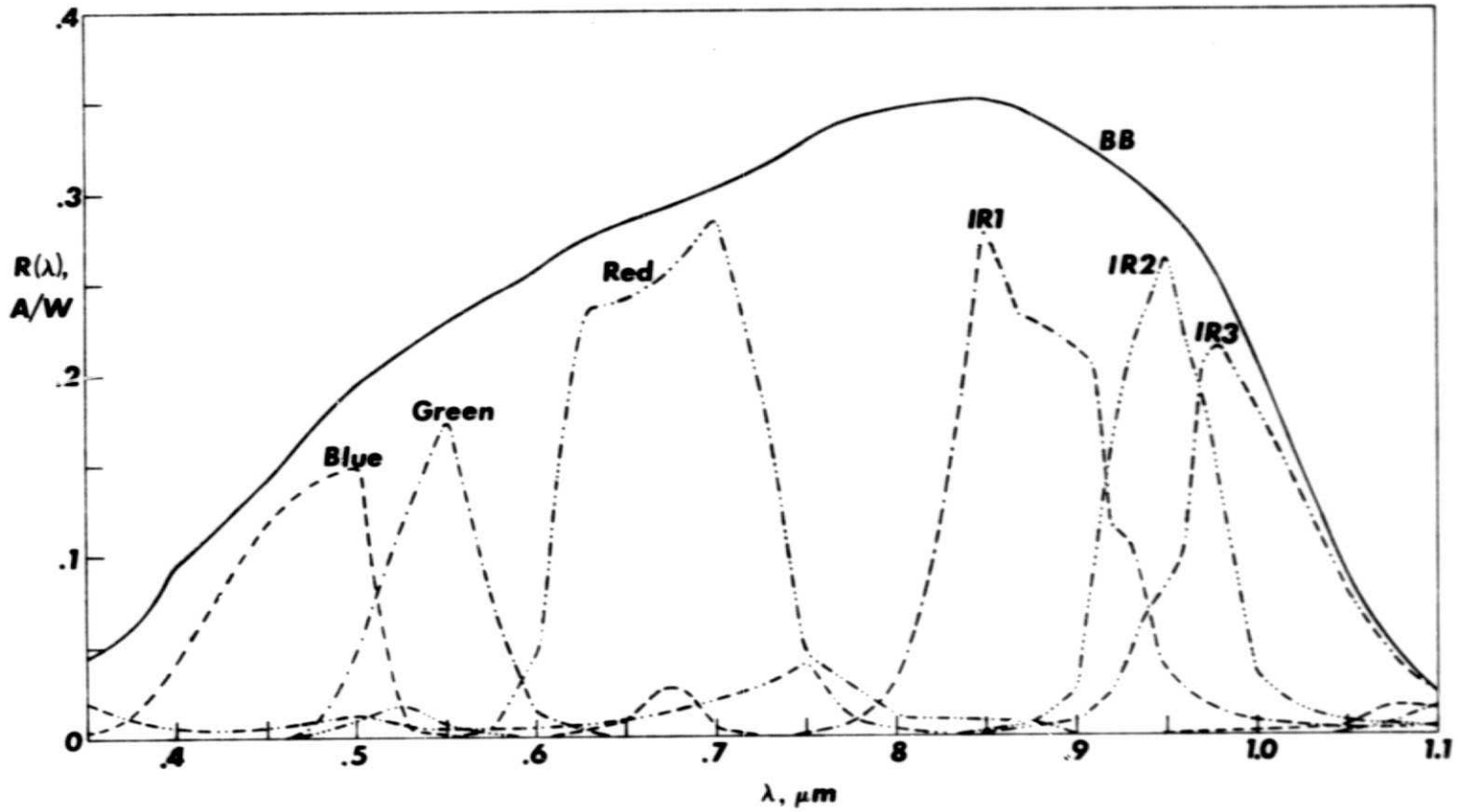

Figure 2.- Typical photosensor array responsivities.

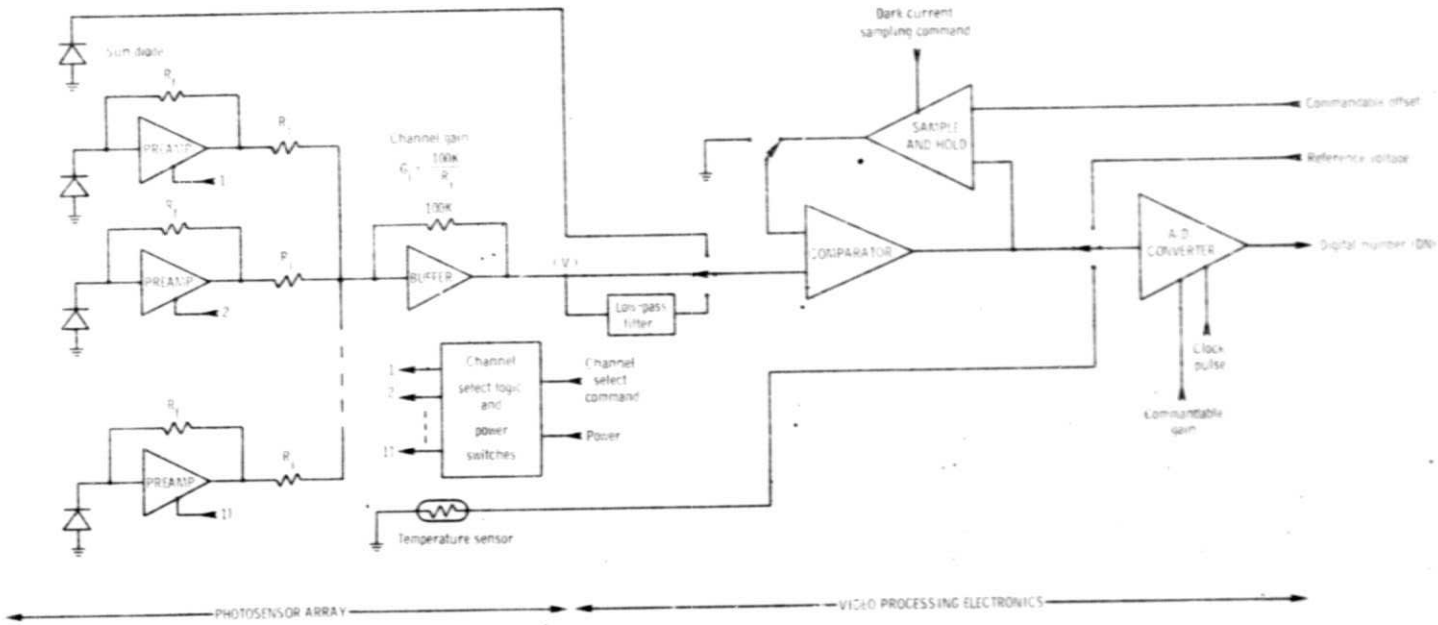

Figure 3.- Simplified circuit diagram of the photosensor array (PSA) and video processing electronics (VPE).

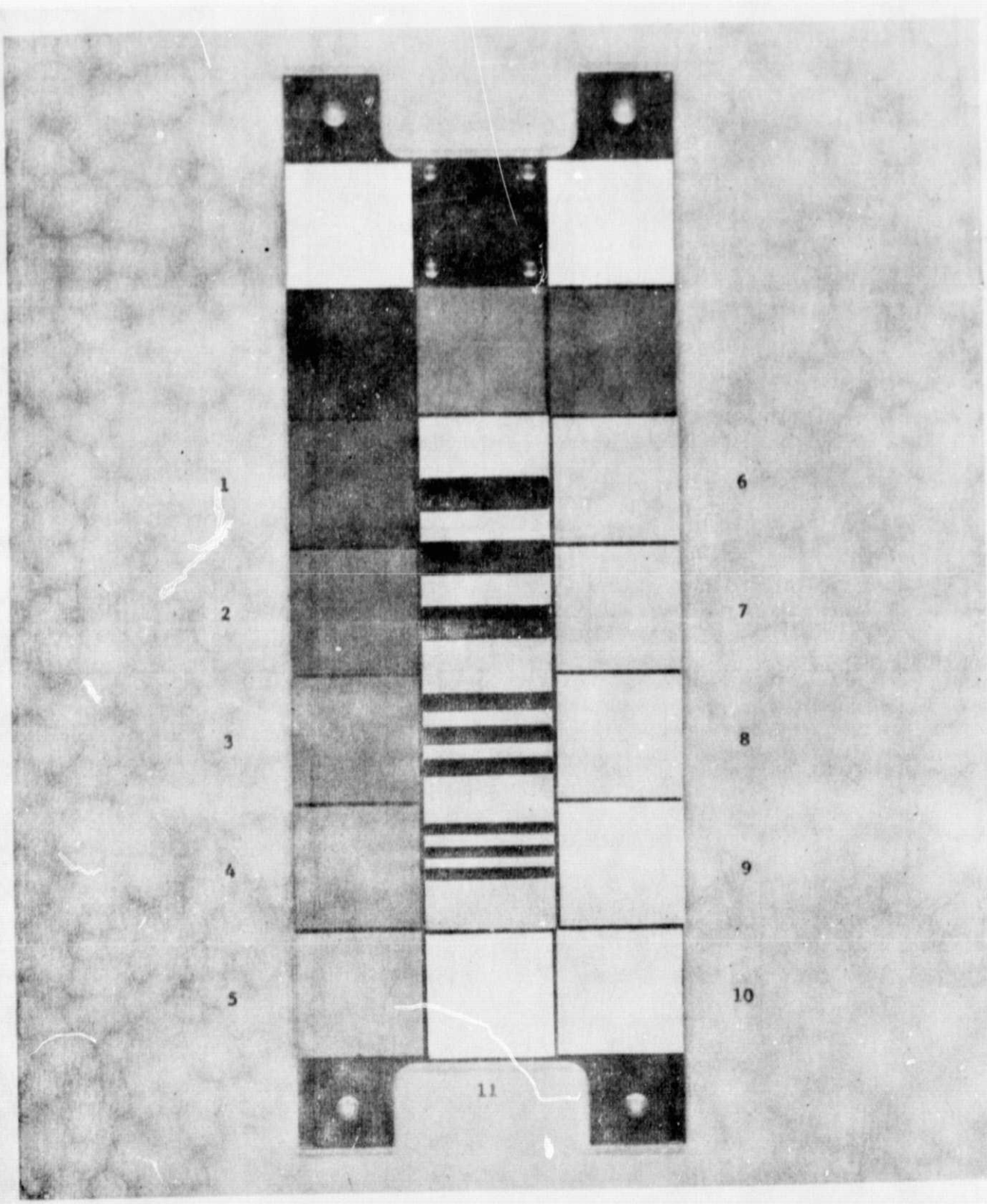

NASA
L-74-2406

Figure 4.- Reference test chart.

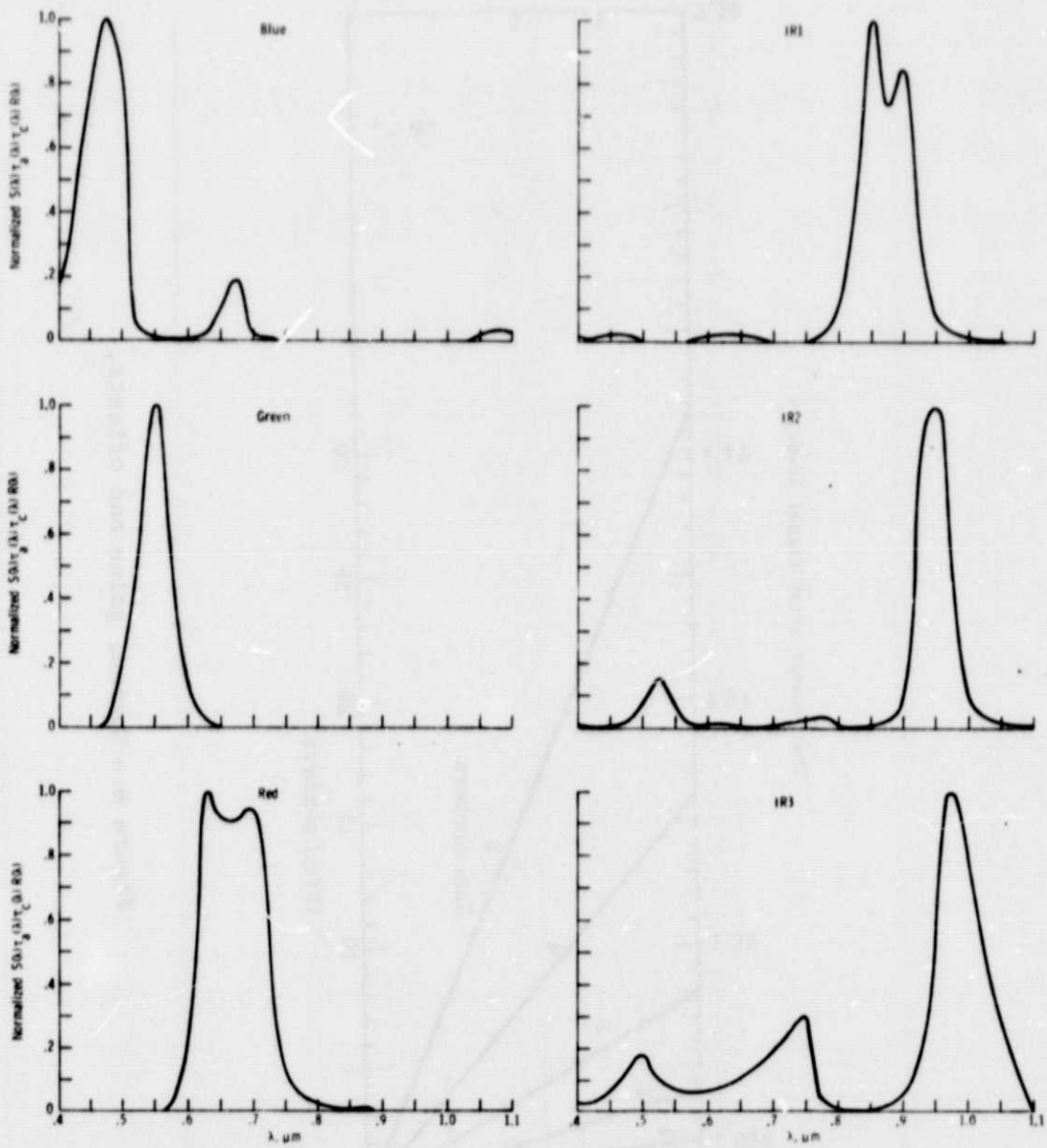

Figure 5.- Variation of the product of solar irradiance, atmospheric transmissivity, optical throughput, and photosensor array responsivity with wavelength.

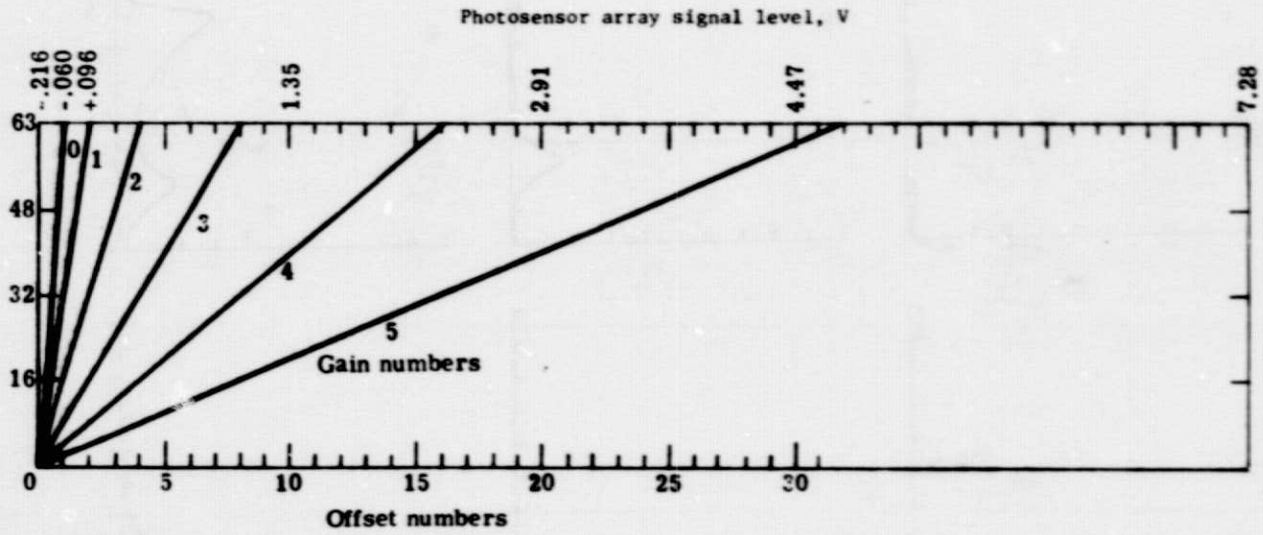

Figure 6.- Nominal gains and offsets.

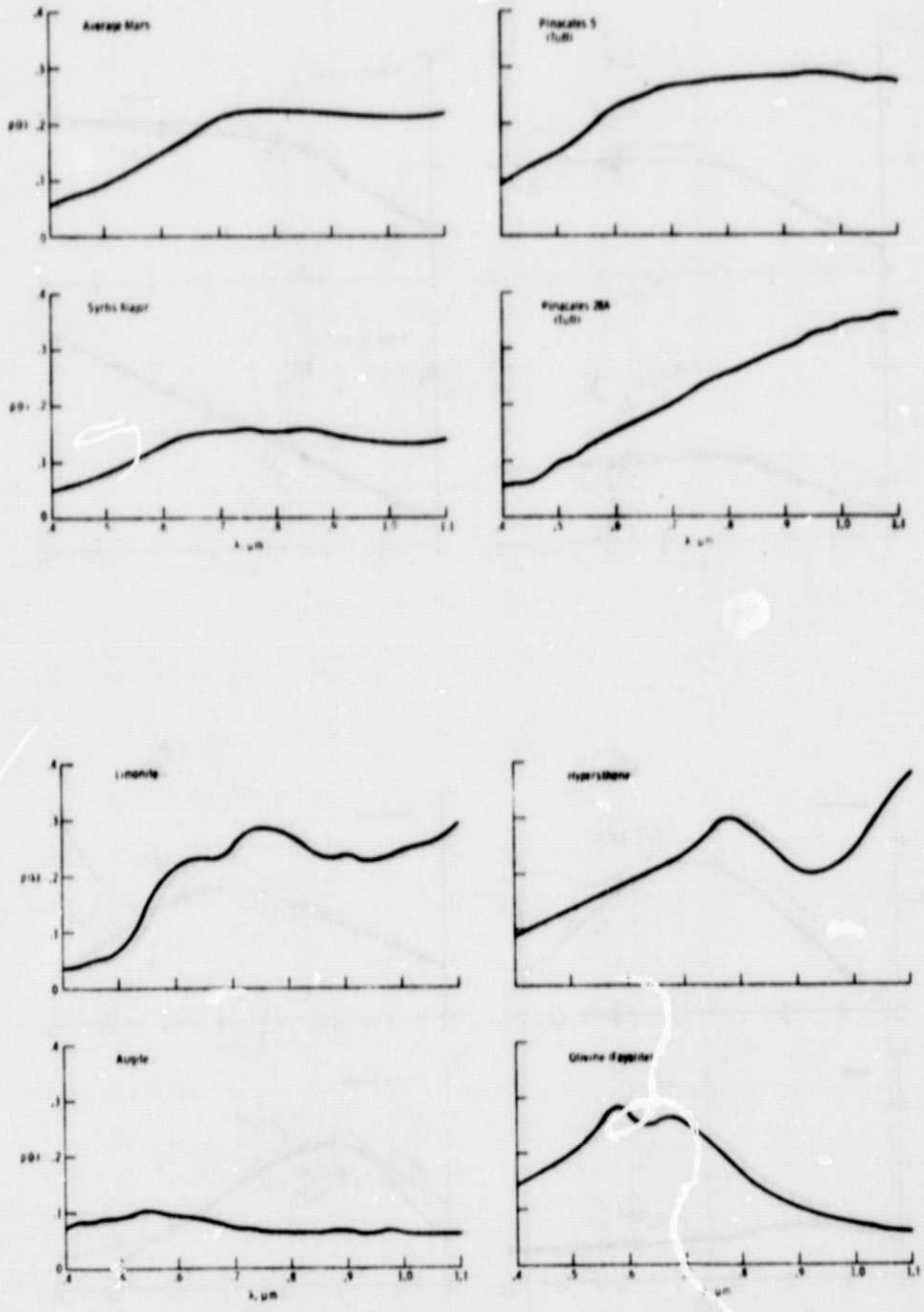

Figure 7. - Spectral reflectances of geological materials considered as inputs.

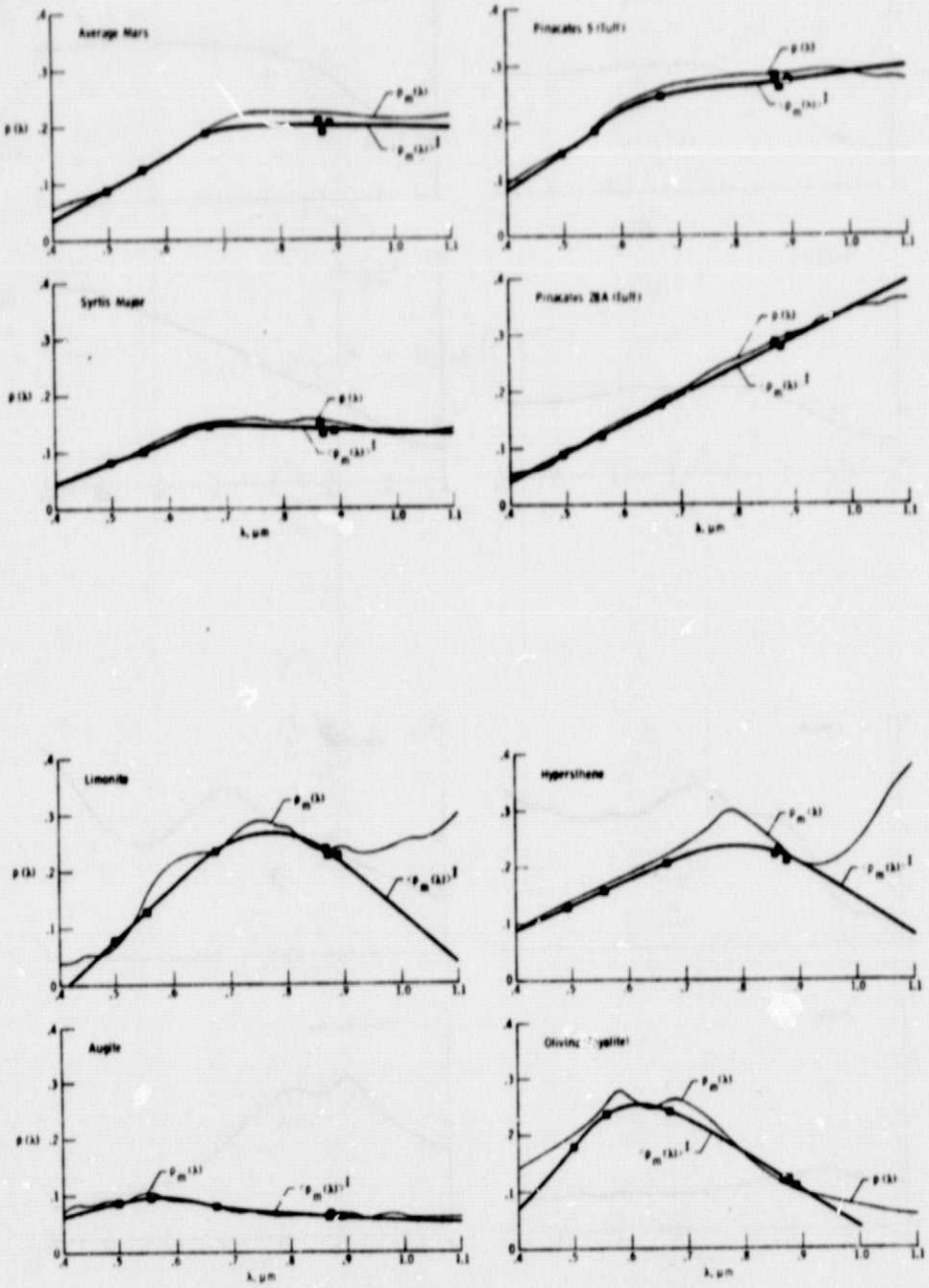

Figure 8. - First-order reflectance values plotted near the peak in-band response of each channel.

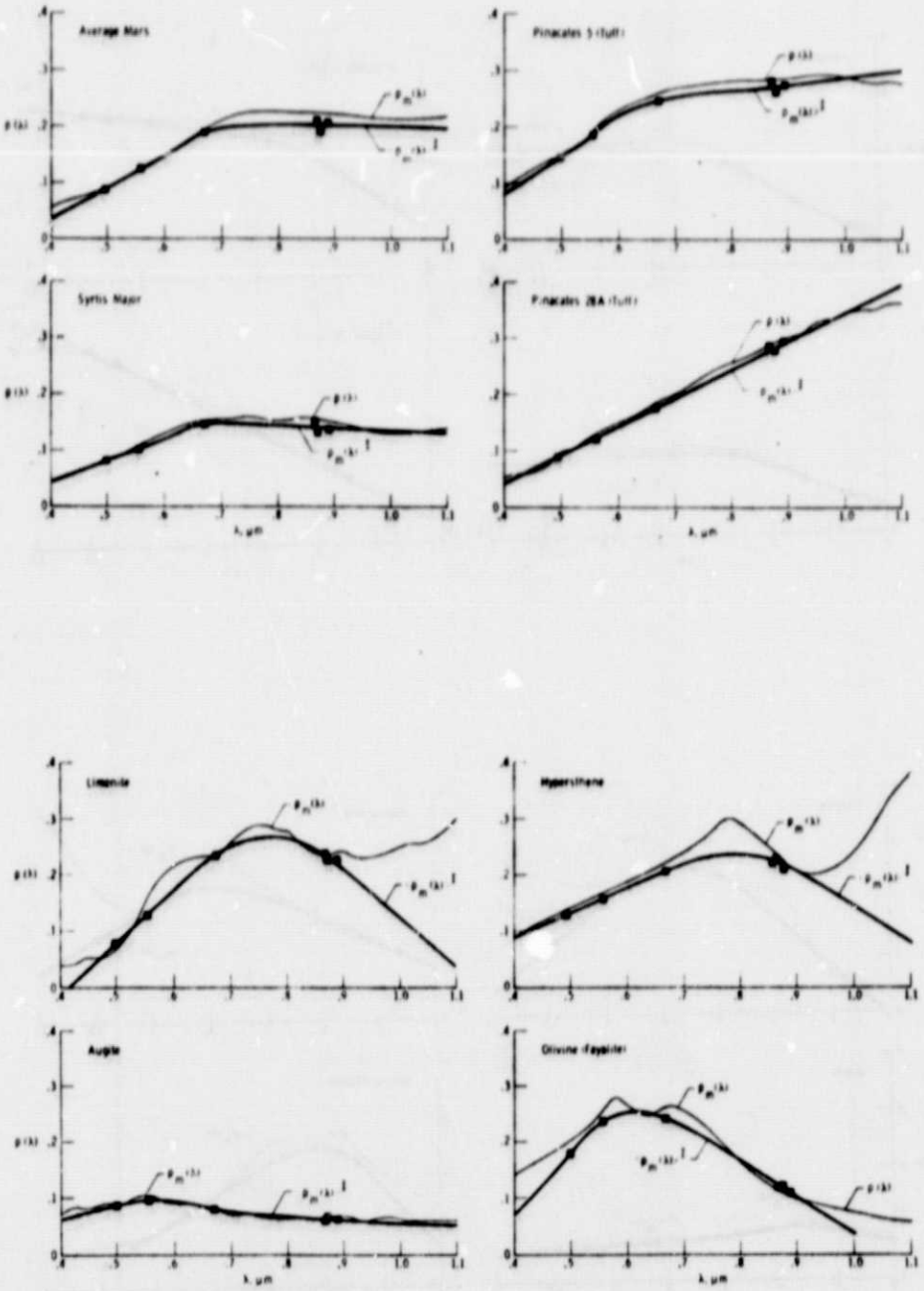

Figure 9. - First-order reflectance values plotted at surface-irradiance and camera-respons'vity weighted wavelengths for each channel.

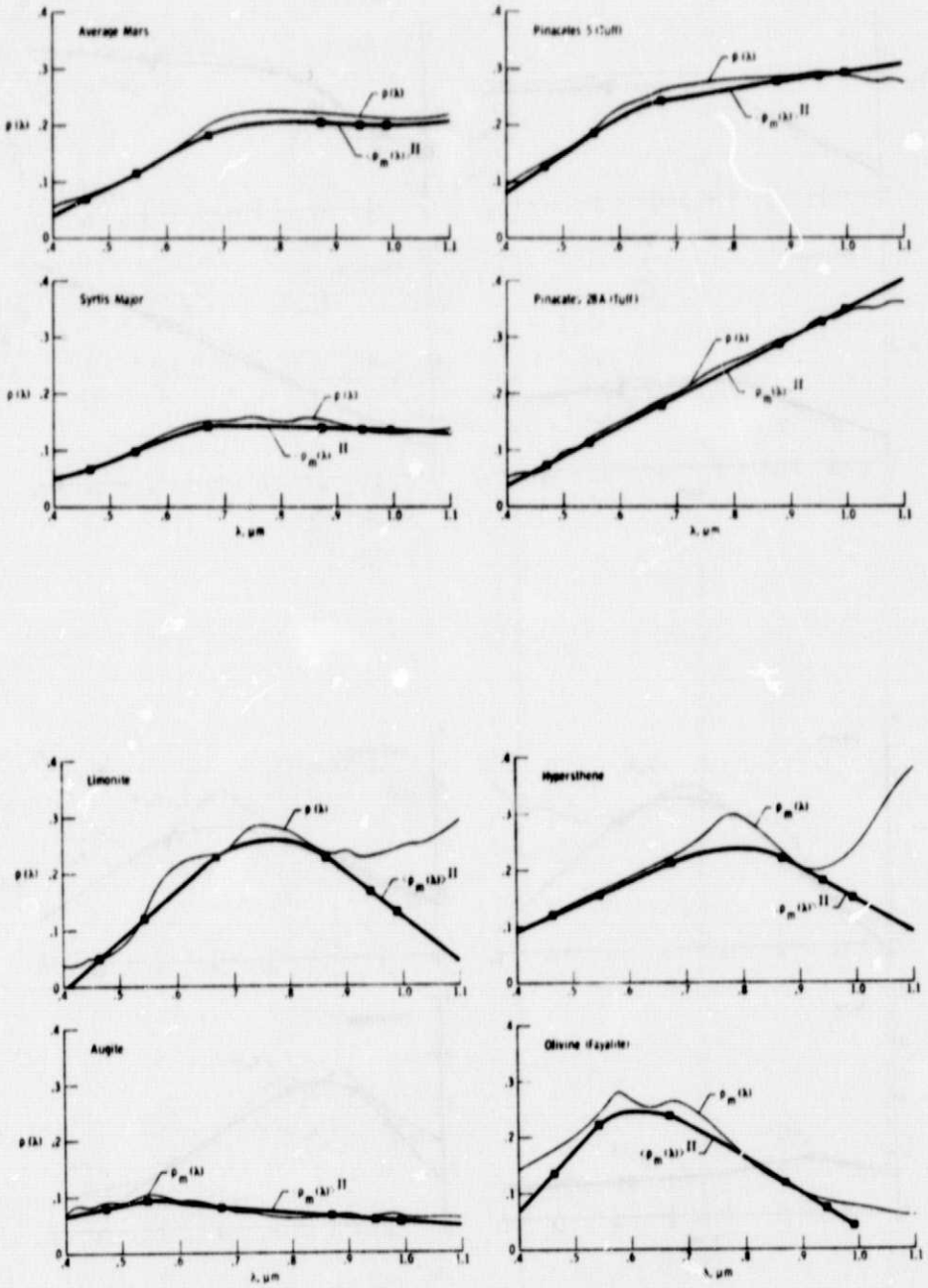

Figure 10. - Second-order reflectance values plotted at in-band surface-irradiance and camera-responsivity weighted wavelengths for each channel.